Journal of Materials Science & Technology 237 (2025) 268–274

Contents lists available at ScienceDirect

Journal of Materials Science & Technology

journal homepage: www.elsevier.com/locate/jmst

Letter

Pressure-induced structural evolution in dual-phase rare-earth high-entropy alloy with significantly different compressibility between two phases

1. Introduction

Compared with the widely used vapor-compression refrigeration, solid-state cooling based on phase transition offers higher efficiency, environmental friendliness, and smaller volume [1,2]. The phase transition of solid refrigerants can be triggered by external fields, i.e., magnetic fields [3–5], electric fields [6,7], and mechanical fields induced by hydrostatic pressure [8] and uniaxial stress [9]. Hysteresis is commonly recognized as a primary limiting factor in the development of materials with first-order phase transitions [10,11]. The second-order phase transition materials offer an effective solution to this challenge, due to their minimal hysteresis during phase transition processes [11]. High-entropy alloys (HEAs), as a novel class of materials, generally comprise more than four components and contain equimolar compositions [12–14]. A large number of HEAs have been explored, exhibiting second-order magnetic phase transitions and comparable magnetocaloric properties [15,16]. Owing to relatively high magnetocaloric responses, rare-earth HEAs (RE-HEAs) have garnered considerable interest among the explored HEA systems [15–19]. $Gd_{20}Tb_{20}Dy_{20}Ho_{20}Er_{20}$, drawing most attention in the magnetocaloric HEA community, exhibits a second-order magnetic transition, a peak value of magnetic entropy change ($|\Delta S_M^{pk}|$) of 8.6 J kg^{-1} K^{-1}, a temperature averaged entropy change (*TEC*(10)) of 8.4 J kg^{-1} K^{-1}, and a refrigeration capacity (*RC*) of 627 J kg^{-1} under a magnetic field change ($\mu_0\Delta H$) of 5 T [19,20]. However, the performance limitations of RE-HEAs, such as lower isothermal entropy change values compared to those of many first-order phase transition materials [1,16,21], and smaller *TEC*(10) and *RC* values than those of many RE-based alloys [1,22–24], largely restrict their application in the field of refrigeration.

RE magnetocaloric materials with a multi-phase structure and multiple magnetic transition temperatures show relatively large maximum magnetic entropy change over a wide working temperature range, resulting in enhanced *TEC*(10) and *RC* [25–28]. The Gibbs free energy of mixing, ΔG_{mix}, can be expressed as follows, $\Delta G_{mix} = \Delta H_{mix} - T\Delta S_{mix}$, where ΔH_{mix}, ΔS_{mix}, and T represent mixing enthalpy, mixing entropy, and temperature, respectively. The alloy system becomes unstable when ΔS_{mix} decreases while ΔH_{mix} remains constant [29]. The heat of mixing (ΔH_{AB}^{mix}) between Gd, Tb, Dy, Ho, and Er is 0 [30]. Therefore, reducing the number of constituent elements in the RE-HEA to decrease its ΔS_{mix} would facilitate the preparation of a multi-phase structure. Additionally, the melt-extraction technology is effective for preparing multi-phase microwires due to the significant difference in cooling rates of the free surface and the region contacting with the wheel during the preparation process. This has been demonstrated in our previous work [27].

Based on the above characteristics of the influence of composition design and the preparation process on the structure of high-entropy alloys, as well as the $Gd_{20}Tb_{20}Dy_{20}Ho_{20}Er_{20}$ composition, we designed and fabricated $Gd_{25}Tb_{25}Dy_{25}Ho_{25}$ and $Gd_{25}Dy_{25}Ho_{25}Er_{25}$ microwires using melt-extraction technology, as shown in Fig. S1 in Supporting Information. The bright-field transmission electron microscopy (TEM) images shown in Fig. 1(a, b) illustrate that the $Gd_{25}Tb_{25}Dy_{25}Ho_{25}$ alloy exhibits a dual-phase structure, consisting of a matrix and a uniformly distributed nanocrystalline secondary phase. The selected area electron diffraction (SAED) results corresponding to Fig. 1(b), shown in Fig. 1(c), confirm that the matrix and secondary phase have hexagonal-close-packed (hcp, $[01\bar{1}0]$ zone axis) and face-centered-cubic (fcc, $[\bar{1}12]$ zone axis) structures, respectively. The dual-phase structure of the $Gd_{25}Dy_{25}Ho_{25}Er_{25}$ alloy is confirmed by the TEM images shown in Fig. S2. In Fig. S3, the $Gd_{25}Tb_{25}Dy_{25}Ho_{25}$ alloy shows a$|\Delta S_M^{pk}|$ value of 10.8 J kg^{-1} K^{-1} (5 T), a *TEC*(10) value of 10.5 J kg^{-1} K^{-1} (5 T), an *RC* value of 507 J kg^{-1}, and a second-order magnetic phase transition. The $|\Delta S_M^{pk}|$, *TEC*(10) and *RC* values of the $Gd_{25}Dy_{25}Ho_{25}Er_{25}$ alloy are 7.6 J kg^{-1} K^{-1}, 7.5 J kg^{-1} K^{-1} and 889 J kg^{-1}, respectively, at $\mu_0\Delta H = 5$ T However, the $Gd_{25}Dy_{25}Ho_{25}Er_{25}$ alloy exhibits a first-order magnetic phase transition under low $\mu_0\Delta H$. In addition, the performances of the $Gd_{25}Tb_{25}Dy_{25}Ho_{25}$ and $Gd_{25}Dy_{25}Ho_{25}Er_{25}$ alloys remain lower than those of high-performance (i) magnetocaloric materials, which exhibit magnetic entropy change exceeding 20 J kg^{-1} K^{-1} under the same conditions [1], and (ii) barocaloric materials, triggered by hydrostatic pressure, with entropy changes reaching hundreds [21].

By combining multiple field-induced phase transitions, multicaloric materials could achieve the thermal properties, i.e., isothermal entropy and adiabatic temperature changes, that surpass those attainable under the application of a single field [11]. For example, phase transitions, driven by a magnetic field and a compressive load, lead to a higher isothermal entropy change than that induced solely by the magnetocaloric effect [31–33]. In addition, multicaloric cooling offers potential benefits, including widening the operating temperature window, enhancing *RC* and reducing the driving field [11]. During each phase transition of the caloric alloys, heat is either absorbed from or released into the surrounding environment [1,34]. Therefore, under isothermal conditions, when pressure induces multiple phase transitions in an alloy, each transition produces a certain entropy change value. There is a high probability that inducing as many phase transitions as possible through pressure and superimposing the corresponding thermal properties will significantly increase the overall isothermal entropy change. Investigating the combined effects of magnetic fields and compressive loads on multi-phase RE-HEAs, as well as how to induce as many phase transitions as possible, is of great significance for

https://doi.org/10.1016/j.jmst.2025.03.027

furthering the application of RE-HEAs in refrigeration. Understanding the structural evolution under compression is critical for advancing this research.

High pressure applied by a diamond anvil cell (DAC) can directly vary the volume per atom of a crystal, leading to changes in its electronic structure and valence state. This could result in phase transitions of RE metals and alloys [35,36]. In the RE-HEA field, only the $Gd_{20}Tb_{20}Dy_{20}Ho_{20}Y_{20}$ alloy has been compressed using a DAC, exhibiting the phase transition sequence of hcp → samarium-type (Sm-type) → double hcp (dhcp) → distorted fcc (dfcc) under compression up to 60.1 GPa [36]. For the elements composing the alloy under the same compression conditions, Gd, Tb, and Dy exhibit the appearance of an fcc phase during the hcp to dfcc phase transition. The specific phase transition sequence is hcp → Sm-type → dhcp → fcc → dfcc [37–40]. The fcc phase was not observed in the phase transition sequence of Ho and Y [35,41–43]. It is unclear whether the absence of the fcc phase in the phase transition sequence of the $Gd_{20}Tb_{20}Dy_{20}Ho_{20}Y_{20}$ alloy is due to the individual or combined effects of Ho and Y. In addition, the phase transition behavior and the influence of phase interfaces, secondary phase content and size, and energy fluctuations on the microstructural evolution of the dual-phase RE-HEAs under high pressure remain uncertain.

The phase transition pressure values of lanthanide RE elements increase with increasing atomic number, thus the Er element has a relatively high phase transition pressure value [42]. This impedes the RE-HEA from undergoing as many phase transitions as possible under high pressure. The $Gd_{25}Tb_{25}Dy_{25}Ho_{25}$ alloy allows for a precise analysis of the effect of Ho on the phase transition behavior of RE-HEAs. In addition, $Gd_{25}Tb_{25}Dy_{25}Ho_{25}$ alloy exhibits a second-order magnetic phase transition. Therefore, the $Gd_{25}Tb_{25}Dy_{25}Ho_{25}$ alloy was selected and compressed up to 52.15 GPa by a DAC. The mechanisms of the phase transition and microstructural evolution were studied using *in-situ* synchrotron radiation X-ray diffraction (XRD) and *ex-situ* TEM. It can be expected that this study would be helpful for exploring the HEA suitable for solid-state cooling systems.

2. Results and discussion

The material preparation and experimental methods are described in the Supporting Information. Based on Fig. 1(a), the grain size frequency distribution analysis of the matrix of $Gd_{25}Tb_{25}Dy_{25}Ho_{25}$ alloy is shown in Fig. S4, indicating an average grain size of 852 nm. In addition, Fig. 1(a), together with Fig. S5, confirms that the pre-deformed alloy exhibits a low dislocation density. The fraction and grain size of the secondary phase are about 4.5 % and 14 nm (Fig. S6), respectively. Fig. S7 indicates that the secondary phase is semi-coherent with the matrix.

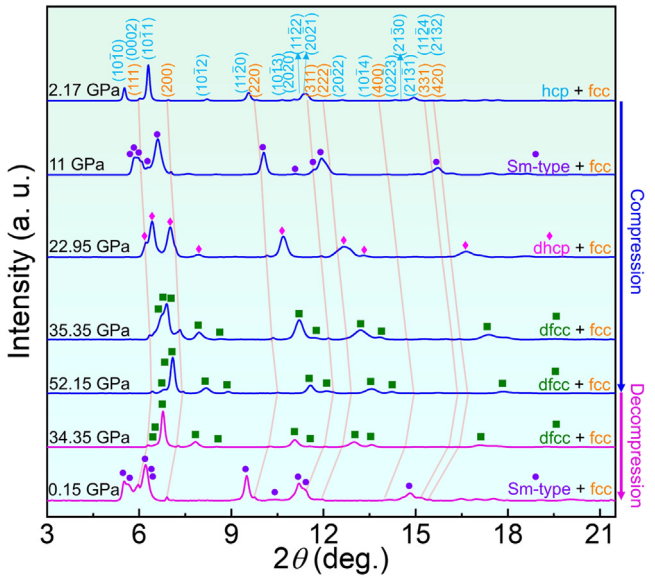

Fig. 2. The representative XRD patterns of the $Gd_{25}Tb_{25}Dy_{25}Ho_{25}$ alloy during compression to 52.15 GPa and decompression down to 0.15 GPa; the patterns during compression show the hcp and fcc phases at 2.17 GPa, the Sm-type and fcc phases at 11 GPa, the dhcp and fcc phases at 22.95 GPa, and the dfcc and fcc phases at 35.35 and 52.15 GPa; the patterns during decompression indicate the dfcc and fcc phases at 34.35 GPa, and the Sm-type and fcc phases at 0.15 GPa; the hcp, Sm-type, dhcp, and dfcc phases observed in the matrix during the phase transition are represented by blue text, purple circles, magenta diamonds, and green squares, respectively; the fcc phase, identified by orange text and lines, remains as the secondary phase throughout the compression-decompression cycle.

All *in-situ* high-pressure XRD patterns during both compression and decompression processes are presented in Fig. S8. Fig. 2 shows the representative XRD patterns. The evolutions of the phase structure and volume per atom of the studied alloy during the compression-decompression cycle are obtained from the refined XRD patterns, as shown in Fig. S9. At the initial pressure, 2.17 GPa, diffraction peaks of two phases can be confirmed. The space groups of $P6_3/mmc$ and $Fm\bar{3}m$ correspond to the matrix with hcp structure and the secondary phase with fcc structure, respectively. The orange lines in Fig. 2 illustrate the peak position evolution of the secondary fcc phase during the compression-decompression cycle. Throughout the entire cycle, the secondary fcc phase exhibits no phase transition. During compression, all the

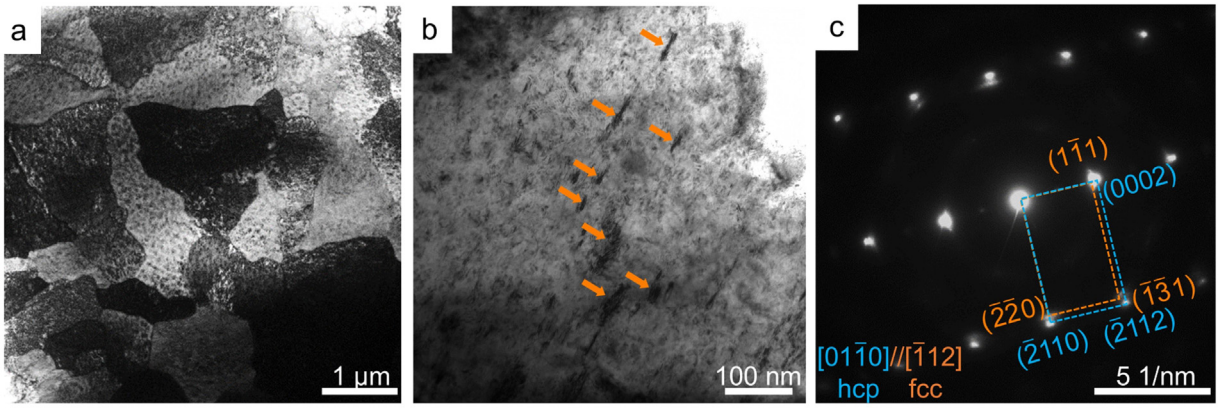

Fig. 1. TEM images of the $Gd_{25}Tb_{25}Dy_{25}Ho_{25}$ alloy: (a) Low-magnification bright-field image; (b) high-magnification bright-field image; the orange arrows in (b) indicate the regions corresponding to the secondary phase with nanometer grain sizes; (c) the corresponding SAED pattern of (b).

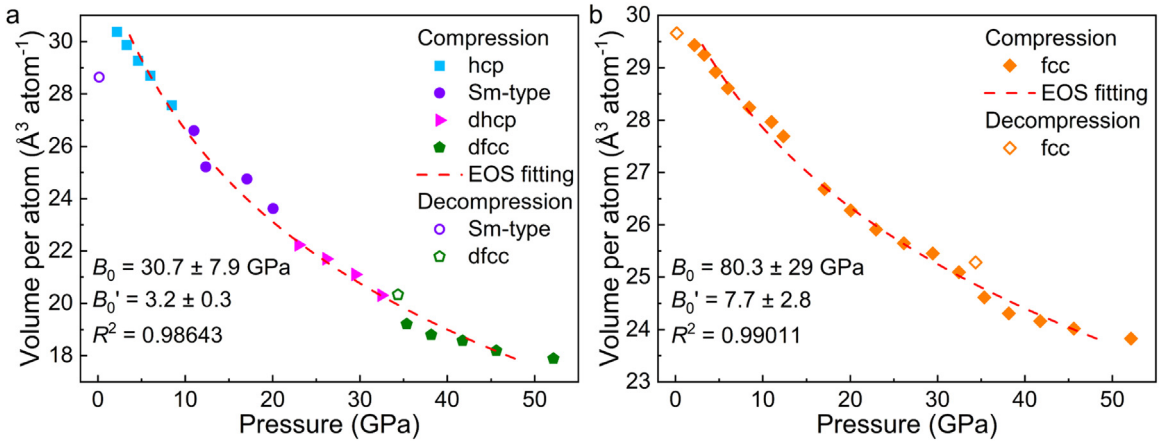

Fig. 3. Volume per atom as a function of pressure for (a) the matrix and (b) the secondary fcc phase of the $Gd_{25}Tb_{25}Dy_{25}Ho_{25}$ alloy, with the Birch-Murnaghan EOS fitting results shown as red dashed lines.

diffraction peaks of both the matrix and secondary phase shift towards higher diffraction angles, indicating a volume decrease of the studied alloy [44]. For the matrix, the hcp phase is observed continuously from 2.17 to 8.45 GPa. At 6 GPa, the XRD pattern exhibits the presence of the Sm-type phase, as shown in Fig. S8(a). The Sm-type phase with space group $R\bar{3}m$ persists until 20.05 GPa (Fig. S8(b)). Then, a dhcp phase with space group $P6_3/mmc$ is observed at the pressure range of 22.95–32.45 GPa. Beginning at 29.45 GPa, the dhcp phase is observed to coexist with the dfcc phase (Fig. S8(c)). The space group of dfcc phase is $R\bar{3}m$. Within the pressure range of 35.35–52.15 GPa, the matrix retains the dfcc structure (Fig. S8(d)). As the pressure decreases to 34.35 and 0.15 GPa, the matrix exhibits the dfcc phase and the Sm-type phase, respectively, as shown in Fig. S8(e). During the decompression process, the pressure at which the Sm-type phase reappears is lower than the pressure at which it initially appears during compression, indicating hysteresis in the phase transition of the matrix.

Fig. 3 shows the pressure dependence of volume per atom. The data obtained from the refined XRD patterns during the compression process can be successfully fitted by a third-order Birch-Murnaghan equation of state (EOS) [45], as marked by red dashed lines in Fig. 3. The third-order Birch-Murnaghan EOS can be expressed as follows [45,46]:

$$p = \frac{3}{2}B_0\left[\left(\frac{V_0}{V}\right)^{\frac{7}{3}} - \left(\frac{V_0}{V}\right)^{\frac{5}{3}}\right]\left\{1 + \frac{3}{4}\left(B_0^{'} - 4\right)\left[\left(\frac{V_0}{V}\right)^{\frac{2}{3}} - 1\right]\right\} \quad (1)$$

where B_0 is the isothermal bulk modulus at standard temperature (an indicator for evaluating resistance to bulk compression), B_0' is the pressure derivative of the isothermal bulk modulus at standard temperature, and V_0 is the atomic volume at ambient conditions. The B_0 and B_0'for matrix are determined as 30.7 ± 7.9 GPa and 3.2 ± 0.3, respectively. The B_0 value for the matrix of the studied alloy closely approximates 32.7 GPa, as calculated using the rule of mixture [36,47], i.e., $B_0 = \sum_{i=1}^{n} c_i B_{0i}$, where c_i and B_{0i} represent the atomic percentage and bulk modulus of each RE element, respectively [35,38,40,48]. The secondary fcc phase exhibits B_0 and B_0' values of 80.3 ± 29 GPa and 7.7 ± 2.8, respectively. The B_0 value of the secondary fcc phase is much higher than that of the matrix, indicating that the secondary phase of the studied alloy is much more incompressible than the matrix.

Fig. 4(a, b) shows the bright- and dark-field TEM images, respectively, of the $Gd_{25}Tb_{25}Dy_{25}Ho_{25}$ alloy recovered from 52.15 GPa. The sample preparation process is presented in Fig. S10. The grain size frequency distribution analysis of the matrix of the recovered sample is shown in Fig. S11. This figure illustrates an average grain size of 88 nm, indicating the significant grain refinement of the matrix after the compression-decompression cycle. The energy dispersive spectroscopy (EDS) analysis confirms a uniform distribution of constituent elements in the recovered sample, as shown in Fig. S12. The high-resolution TEM (HRTEM) images of the recovered sample are presented in Fig. 4(c, d). Fig. 4(e, f) displays the fast Fourier transform (FFT) images, corresponding to the blue dashed square in Fig. 4(c) and orange dashed square in Fig. 4(d), respectively. In addition, the high-magnification bright-field TEM image and FFT-inverse FFT image shown in Fig. S13, combined with Fig. 4(a) with Fig. S5, confirm that the dislocation density of the studied alloy significantly increases after the compression-decompression cycle. The diffraction rings in the SAED pattern of the recovered sample, shown in Fig. 4(g), compared with Fig. 1(c), indicate random grain orientations and decreased grain size, consistent with the analysis results from Figs. S4 and S11. Both the FFT images and SAED pattern confirm the hcp structure of the matrix and the fcc structure of the secondary phase in the recovered sample.

In pressure-induced phase transitions of materials, the phase that exists at higher pressure is usually more resistant to compression [35,49]. Jelen et al. [50] stated that $Tb_{20}Dy_{20}Ho_{20}Er_{20}Tm_{20}$ HEA, which possesses a dual-phase structure consisting of an hcp matrix and a secondary cubic close-packed (CCP) phase exhibits slight compositional differences, with the secondary phase being enriched in Y by about 3 % compared to the matrix. The slight compositional difference and mismatch in interplanar spacing between the matrix and the secondary phase in the dual-phase HEA result in strong lattice distortion and mechanical strain at the phase boundary [29,50,51]. The constituent elements of the studied alloy exhibit a phase transition sequence of hcp → Sm-type → dhcp → (fcc) → dfcc. The fcc phase exists at relatively high pressures and tends to exhibit a high resistance to compression. The B_0 value of the matrix in the $Gd_{25}Tb_{25}Dy_{25}Ho_{25}$ alloy is slightly lower than the B_0 value calculated using the rule of mixture. Among the constitute elements of the studied alloys, Dy and Ho exhibit relatively high B_0 values [35,38,40,52]. This suggests that Dy and/or Ho elements are highly prone to exhibit slight segregation in the secondary phase. From Fig. 1(a), the interplanar spacing (d) of the (0002) plane in the hcp phase (d_{0002}) and (111) plane in the fcc phase (d_{111}) are 2.85 Å and 3.06 Å, respectively. The mismatch of d between the hcp and fcc phases can be calculated as $\varepsilon = (d_{0002} - d_{111})/d_{0002}$, yielding a result of $\varepsilon = -7.4$ % [50]. Therefore, the interface between the matrix and the secondary phase in the $Gd_{25}Tb_{25}Dy_{25}Ho_{25}$ alloy exhibits strong mechanical strain and lattice distortion. These serve as micro-interfacial barriers to compressible behavior in HEAs [49].

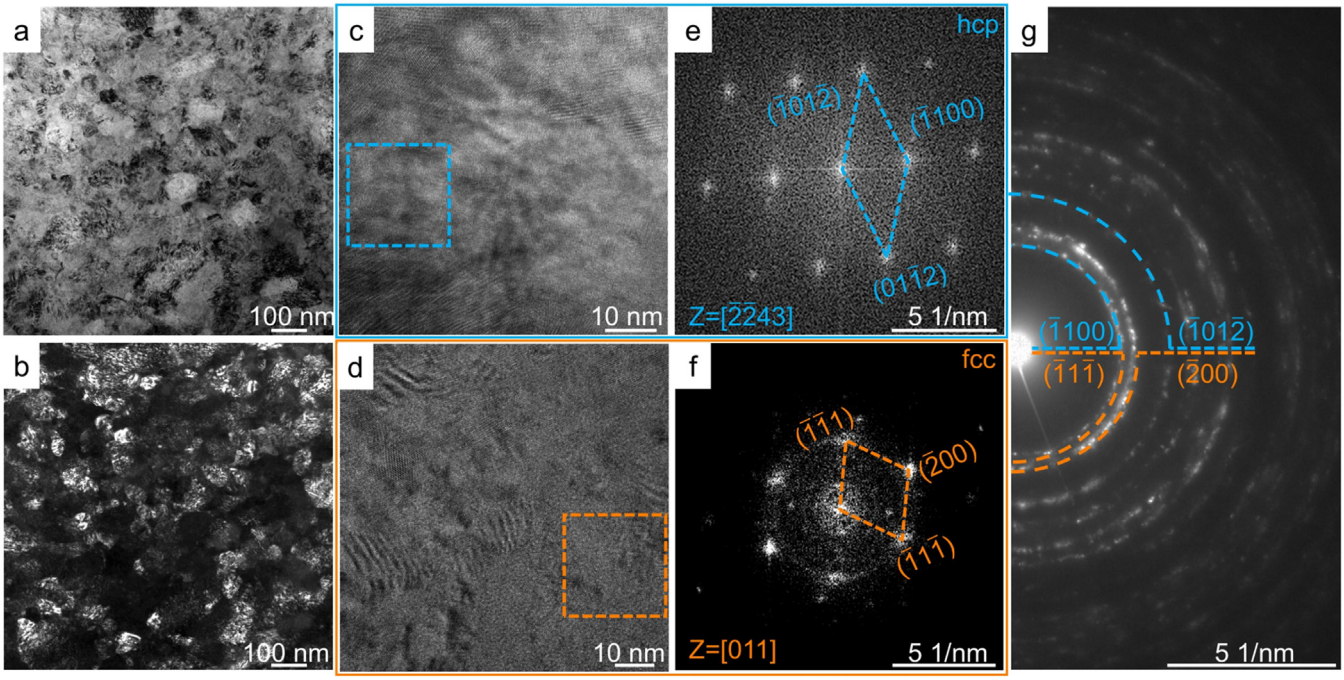

Fig. 4. TEM images of the $Gd_{25}Tb_{25}Dy_{25}Ho_{25}$ alloy recovered from 52.15 GPa: (a) bright-field TEM image; (b) dark-field TEM image; (c, d) HRTEM images; (e, f) corresponding FFT images for the blue and orange dashed squares in (c, d), respectively; (g) SAED pattern.

The secondary phase in the studied alloy exhibits an extremely small grain size compared to the matrix. Consequently, the interface has a significantly greater effect on the compressible behavior of the secondary phase than on that of the matrix. Furthermore, the mismatch in lattice parameters between the matrix and the secondary phase increases with increasing pressure, as shown in Fig. 2, leading to enhanced lattice distortion in the phase boundary [49]. This results in strengthened micro-interfacial barriers and, consequently, a much higher B_0 of the secondary phase compared to that of the matrix [49].

Some previous studies have suggested that the absence of the fcc phase in the phase transition sequence of Ho metal may be due to two reasons: (1) the phase transitions directly from dhcp to dfcc, skipping the fcc phase [41,42], and (2) the fcc phase exists only within a very narrow pressure range (e.g., 3.7 GPa) [35]. The phase transition in RE-HEAs is triggered by an increased number of *d* electrons, originating from the *s* band [36,53]. In contrast to the secondary phase, the matrix exhibits a significantly smaller B_0, resulting in a much higher reduction in volume per atom of the matrix (41.1 %) from 2.17 to 52.15 GPa compared to the secondary phase (19.1 %), as shown in Fig. 3. This facilitates a higher probability for $s \rightarrow d$ charge transfer in atoms within the matrix, thereby triggering the phase transitions in the matrix [36]. The absence of a phase transition in the secondary phase may be due to either (1) the insufficient reduction in volume per atom to induce the $s \rightarrow d$ charge transfer, or (2) the number of electrons transferred from *s* to *d* bands not being sufficient to trigger the phase transition. The elements constituting HEAs play a crucial role in influencing the structures [54]. The absence of the fcc phase in the phase transition sequence of the matrix during compression may be due to the presence of the Ho element, which could lead to either (1) a direct transformation from dhcp to dfcc, or (2) the fcc phase existing within a narrow pressure range, resulting in it being missed during observation. Fig. 5 shows a schematic diagram of the microstructural evolution of the $Gd_{25}Tb_{25}Dy_{25}Ho_{25}$ alloy during compression. The plastic deformation in the HEA occurs through dislocation motion and multiplication [55,56]. Xiong et al. [37] reported that the heavy RE metal undergoes plastic deformation under pressure applied in a DAC at room temperature when exceeding 16 GPa. In this study, the pressure was applied up to 52.15 GPa, resulting in severe deformation of the $Gd_{25}Tb_{25}Dy_{25}Ho_{25}$ alloy through significant dislocation multiplication and movement.

Typically, the interaction between dislocations and a secondary phase occurs in two ways: cutting through or bowing around (Orowan dislocation bypassing). There is an empirical rule that when the secondary phase grain size is small, dislocations tend to cut through them, whereas for large secondary phase grains, bowing may dominate [57]. However, this treatment does not take into account other factors. For example, if the second phase is incoherent with the matrix, bowing will dominate [57–59]. If the second phase is coherent or semi-coherent with the matrix, the dominant interaction model can be identified by calculating and comparing the yield-strengthening contributions of both models [60,61]. Alternatively, in the second condition, the dominant model can be determined by calculating the surface energy and shear modulus based on the two models and evaluating the reasonableness of the obtained values [57]. Due to limited material parameters, it is difficult to calculate the above parameters for the studied alloy. Soler et al. reported that $Gd_{20}Tb_{20}Dy_{20}Ho_{20}Y_{20}$ HEA consists of a matrix and a homogeneously distributed secondary phase, with the secondary phase possessing a fraction and an average grain size of approximately 1.6 % and 10 nm [57]. They obtained the surface energy of the secondary phase to be $\gamma \approx 150$ mJ m^{-2} and shear modulus of the matrix to be $G \approx 12$ GPa. These values are close to those obtained by calculating the values based on the constituent elements and the rule of mixture. This prevents them from determining which model is dominant. The $Gd_{25}Tb_{25}Dy_{25}Ho_{25}$ alloy has a composition similar to that in the aforementioned alloy and exhibits a comparable secondary phase structure, i.e., similar content and grain size. Two alloys may exhibit similar interaction models, such as cutting through, bowing around, or coexistence of both models. The increased mismatch in lattice parameters of the $Gd_{25}Tb_{25}Dy_{25}Ho_{25}$ alloy, induced by increasing pressure, leads to dislocations bypassing the secondary phase.

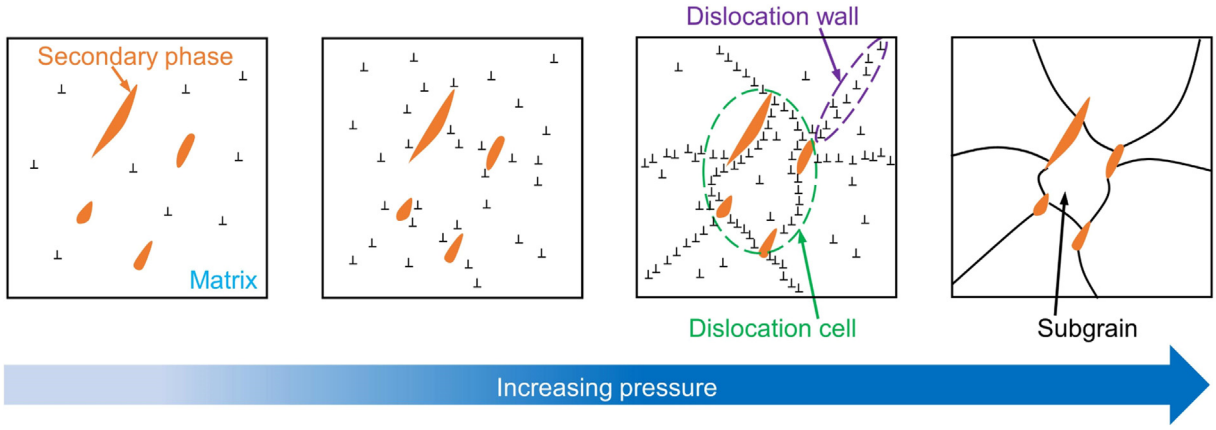

Fig. 5. Schematic diagram of the microstructural evolution of the $Gd_{25}Tb_{25}Dy_{25}Ho_{25}$ alloy during compression.

The enhanced lattice distortion leads to significantly increased interfacial energy at the boundary between the two phases with increasing pressure. In addition, HEAs possess intrinsic lattice distortion [54]. During large deformation, dislocations in the $Gd_{25}Tb_{25}Dy_{25}Ho_{25}$ alloy with different energy states are compelled to shift through these energy-fluctuating distorted lattices. In this process, both distorted lattices and low-energy dislocations act as obstacles, leading to dislocation accumulation and the subsequent formation of dislocation walls and dislocation cells [54,62]. The edges of dislocation cells tend to evolve into low-angle and high-angle grain boundaries (Fig. S13), resulting in the formation of subgrains within the coarse grains [63]. Consequently, the dislocation cells reduce the grain size of the matrix in the studied alloy by forming subgrains. The two-phase coexistence during the transition and the observed hysteresis jointly confirm the pressure-induced first-order phase transition of the matrix of the studied alloy. The shortcomings of first-order phase transition in multicaloric materials, particularly irreversibility induced by the hysteresis, can be overcome by applying multiple fields [11,34,64]. The $Gd_{25}Tb_{25}Dy_{25}Ho_{25}$ alloy exhibits comparable magnetocaloric properties. It can be expected that the simultaneous application of a compressive load and a magnetic field would improve the thermal properties and suppress the pressure-induced phase transition hysteresis of the $Gd_{25}Tb_{25}Dy_{25}Ho_{25}$ alloy.

3. Conclusions

In-situ high-pressure X-ray diffraction and *ex-situ* TEM were conducted to analyze the structural evolution of dual-phase $Gd_{25}Tb_{25}Dy_{25}Ho_{25}$ alloy during the compression-decompression cycle. The studied alloy consists of an hcp matrix and a secondary fcc phase, which has a fraction of ~4.5 % and a grain size ~14 nm. The secondary phase is semi-coherent with the matrix. During compression, the phase transition sequence of the matrix is hcp → Sm-type → dhcp → dfcc while the secondary fcc phase does not undergo any phase transitions. After the compression-decompression cycle, the structure of the matrix recovers to the hcp phase. The B_0 of the secondary fcc phase is much higher than that of the matrix. Under high applied pressure, up to 52.15 GPa, the alloy undergoes severe plastic deformation through significant dislocation multiplication and movement. With increasing pressure, the lattice parameter mismatch between the two phases of $Gd_{25}Tb_{25}Dy_{25}Ho_{25}$ alloy grows, causing dislocations to bypass the secondary phase during compression. The studied alloy possesses energy-fluctuating distorted lattices both intrinsically and at the boundary between the two phases during compression. Therefore, during the large deformation induced by pressure, dislocation movement is hindered by distorted lattices and low-energy dislocations. This leads to the formation of dislocation walls and dislocation cells. The edges of dislocation cells tend to evolve into low-angle and high-angle grain boundaries, resulting in the formation of subgrains and a significant decrease in the grain size of the matrix. These results might shed light on the understanding of the structural evolution of dual-phase high-entropy alloys under high-pressure conditions and provide a strategy for exploring multicaloric materials.

See the Supporting Information for details on the sample preparation method, microstructure and chemistry characterization, and *in-situ* high-pressure XRD.

Declaration of competing interest

The authors declare that they have no known competing financial interests or personal relationships that could have appeared to influence the work reported in this paper.

CRediT authorship contribution statement

Hangboce Yin: Writing – original draft, Investigation, Formal analysis, Data curation. **Jun-Qiang Wang:** Supervision, Funding acquisition. **Kai Zhang:** Writing – review & editing, Supervision, Investigation. **Shu Guo:** Supervision, Investigation. **Nana Li:** Investigation. **Wujing Fu:** Investigation. **Juntao Huo:** Writing – review & editing, Supervision, Funding acquisition. **Jianfei Sun:** Supervision. **Wenge Yang:** Supervision. **Yongjiang Huang:** Writing – review & editing, Supervision, Funding acquisition.

Acknowledgements

This work was financially supported by the National Natural Science Foundation of China (Nos. 52371106, 52371025, 52171154, 51871076, 52071118, and 52301223), Interdisciplinary Research Foundation of HIT (No. IR2021201), and the Natural Science Foundation of Ningbo City (No. 2023J346). This research was supported by Zhejiang Provincial Natural Science Foundation of China (No. LQ24E010004). The beamline 13-ID-D (GeoSoilEnviroCARS) was supported by the National Science Foundation (NSF)-Earth Sciences (No. EAR-1634415) and the Department of Energy (DOE)-GeoSciences (No. DE-FG02-94ER14466). Advanced Photon Source was supported by DOE-BES (No. DE-AC02-06CH11357).

Supplementary materials

Supplementary material associated with this article can be found, in the online version, at doi:10.1016/j.jmst.2025.03.027.

References

[1] V. Franco, J.S. Blázquez, J.J. Ipus, J.Y. Law, L.M. Moreno-Ramírez, A. Conde, Prog. Mater. Sci. 93 (2018) 112–232.
[2] R. Wang, S.L. Fang, Y.C. Xiao, E.L. Gao, N. Jiang, Y.W. Li, L.L. Mou, Y.N. Shen, W.B. Zhao, S.T. Li, A.F. Fonseca, D.S. Galvão, M.M. Chen, W.Q. He, K.Q. Yu, H.B. Lu, X.M. Wang, D. Qian, A.E. Aliev, N. Li, C.S. Haines, Z.S. Liu, J.K. Mu, Z. Wang, S.G. Yin, M.D. Lima, B.G. An, X. Zhou, Z.F. Liu, R.H. Baughman, Science 366 (2019) 216–221.
[3] J.L. Lin, X. Wang, F.Y. Chen, H.F. Li, L.W. Li, J. Mater. Sci. Technol. 207 (2025) 317–323.
[4] H.C. Xie, X.D. Lv, Z.J. Mo, J. Gong, X.Q. Gao, Z.X. Li, J.Q. Wu, J. Shen, J. Mater. Sci. Technol. 193 (2024) 90–97.
[5] Y.K. Zhang, J.Y. Ying, X.Q. Gao, Z.J. Mo, J. Shen, L.W. Li, J. Mater. Sci. Technol. 159 (2023) 163–169.
[6] X. Yang, C.Y. Wang, W.Q. Bao, Z. Li, Z.Y. Wang, J. Feng, Z.H. Ge, J. Mater. Sci. Technol. 217 (2025) 18–28.
[7] S.K. Li, W.G. Zhao, X.L. Shi, L.L. Wang, S.S. Pan, G.F. Cheng, W.D. Liu, M. Li, K. Guo, Z.G. Chen, F. Pan, J. Mater. Sci. Technol. 214 (2025) 194–203.
[8] C.J. Bao, Z.Q. Guan, Z.Z. Li, H.Y. Wang, Y.W. Feng, Q. Guo, K. Zhang, Y.X. Wang, L. Zuo, B. Li, J. Mater. Sci. Technol. 218 (2025) 88–94.
[9] D.Q. Xue, R.H. Yuan, Y.C. Yang, J.B. Pang, Y.M. Zhou, X.D. Ding, T. Lookman, X.B. Ren, J. Sun, D.Z. Xue, J. Mater. Sci. Technol. 103 (2022) 8–14.
[10] X. Moya, N.D. Mathur, Science 370 (2020) 797–803.
[11] H.L. Hou, S.X. Qian, I. Takeuchi, Nat. Rev. Mater. 7 (2022) 633–652.
[12] J.W. Yeh, S.K. Chen, S.J. Lin, J.Y. Gan, T.S. Chin, T.T. Shun, C.H. Tsau, S.Y. Chang, Adv. Eng. Mater. 6 (2004) 299–303.
[13] B. Cantor, I.T.H. Chang, P. Knight, A.J.B. Vincent, Mater. Sci. Eng. A 375-377 (2004) 213–218.
[14] X.H. Yan, Y. Zou, Y. Zhang, Mater. Futures 1 (2022) 022002.
[15] J.Y. Law, V. Franco, J. Mater. Res. 38 (2023) 37–51.
[16] J.Y. Law, V. Franco, APL Mater. 9 (2021) 080702.
[17] L.W. Li, C. Xu, Y. Yuan, S.Q. Zhou, Mater. Res. Lett. 6 (2018) 413–418.
[18] S.F. Lu, L. Ma, J. Wang, Y.S. Du, L. Li, J.T. Zhao, G.H. Rao, J. Alloy. Compd. 874 (2021) 159918.
[19] Y. Yuan, Y. Wu, X. Tong, H. Zhang, H. Wang, X.J. Liu, L. Ma, H.L. Suo, Z.P. Lu, Acta Mater. 125 (2017) 481–489.
[20] L.D. Griffith, Y. Mudryk, J. Slaughter, V.K. Pecharsky, J. Appl. Phys. 123 (2018) 034902.
[21] B. Li, Y. Kawakita, S. Ohira-Kawamura, T. Sugahara, H. Wang, J.F. Wang, Y.N. Chen, S.I. Kawaguchi, S. Kawaguchi, K. Ohara, K. Li, D.H. Yu, R. Mole, T. Hattori, T. Kikuchi, S.I. Yano, Z. Zhang, Z. Zhang, W.J. Ren, S.C. Lin, O. Sakata, K. Nakajima, Z.D. Zhang, Nature 567 (2019) 506–510.
[22] J.S. Liu, M.F. Huang, M.J. Wu, Y. Zhang, G.Y. Cao, Z. Li, H.N. Chen, T.C. Yu, X.F. Wang, R. Liu, G.D. Qu, M.Y. Pang, H.X. Shen, J. Alloy. Compd. 855 (2021) 157231.
[23] Q.Y. Dong, B.G. Shen, J. Chen, J. Shen, F. Wang, H.W. Zhang, J.R. Sun, J. Appl. Phys. 105 (2009) 053908.
[24] Y.K. Zhang, W.X. Hao, J. Shen, Z.J. Mo, T. Gottschall, L.W. Li, Acta Mater. 276 (2024) 120128.
[25] Z. Ma, Y.F. Shang, E. Agurgo Balfour, H. Fu, B.H. Teng, L. Wang, Y. Luo, S.F. Wang, Y.H. Wu, M.G. Han, J. Alloy. Compd. 680 (2016) 268–272.
[26] J.Q. Feng, Y.H. Liu, J.H. Sui, A.N. He, W.X. Xia, W.H. Wang, J.Q. Wang, J.T. Huo, Mater. Today Phys. 21 (2021) 100528.
[27] H.B.C. Yin, J.Y. Law, Y.J. Huang, V. Franco, H.X. Shen, S.D. Jiang, Y. Bao, J.F. Sun, Mater. Des. 206 (2021) 109824.
[28] X.F. Wu, Y.S. Du, X.Q. Gao, F. Liu, L. Ma, G. Cheng, J. Wang, J.T. Zhao, G.H. Rao, J. Alloy. Compd. 1010 (2025) 177742.
[29] Y. Zhang, T.T. Zuo, Z. Tang, M.C. Gao, K.A. Dahmen, P.K. Liaw, Z.P. Lu, Prog. Mater. Sci. 61 (2014) 1–93.
[30] A. Takeuchi, A. Inoue, Mater. Trans. 46 (2005) 2817–2829.
[31] A. Gràcia-Condal, T. Gottschall, L. Pfeuffer, O. Gutfleisch, A. Planes, L. Mañosa, Appl. Phys. Rev. 7 (2020) 041406.
[32] A. Gràcia-Condal, A. Planes, L. Mañosa, Z.Y. Wei, J.P. Guo, D. Soto-Parra, J. Liu, Phys. Rev. Mater. 6 (2022) 084403.
[33] E. Stern-Taulats, T. Castán, L. Mañosa, A. Planes, N.D. Mathur, X. Moya, MRS Bull. 43 (2018) 295–299.
[34] W. Sun, X. Lu, Z.Y. Wei, Q. Li, Z.B. Li, Y.F. Zhang, J. Liu, Addit. Manuf. 59 (2022) 103125.
[35] N.C. Cunningham, W. Qiu, Y.K. Vohra, High Pressure Res. 26 (2006) 43–50.
[36] P.F. Yu, L.J. Zhang, J.L. Ning, M.Z. Ma, X.Y. Zhang, Y.C. Li, P.K. Liaw, G. Li, R.P. Liu, Mater. Lett. 196 (2017) 137–140.
[37] L. Xiong, J. Liu, L.G. Bai, X.D. Li, C.L. Lin, J.F. Lin, J. Appl. Phys. 116 (2014) 243503.
[38] G.K. Samudrala, G.M. Tsoi, S.T. Weir, Y.K. Vohra, High Pressure Res. 34 (2014) 385–391.
[39] N.C. Cunningham, W. Qiu, K.M. Hope, H.P. Liermann, Y.K. Vohra, Phys. Rev. B 76 (2007) 212101.
[40] Y.R. Shen, R.S. Kumar, A.L. Cornelius, M.F. Nicol, Phys. Rev. B 75 (2007) 064109.
[41] M. Pravica, Z. Quine, E. Romano, Phys. Rev. B 74 (2006) 104107.
[42] W.B. Holzapfel, J. Alloy. Compd. 223 (1995) 170–173.
[43] E.J. Pace, S.E. Finnegan, C.V. Storm, M. Stevenson, M.I. McMahon, S.G. MacLeod, E. Plekhanov, N. Bonini, C. Weber, Phys. Rev. B 102 (2020) 094104.
[44] F. Zhang, Y. Wu, H.B. Lou, Z.D. Zeng, V.B. Prakapenka, E. Greenberg, Y. Ren, J.Y. Yan, J.S. Okasinski, X.J. Liu, Y. Liu, Q.S. Zeng, Z.P. Lu, Nat. Commun. 8 (2017) 15687.
[45] F. Birch, J. Geophys. Res. 57 (1952) 227–286.
[46] T. Katsura, Y. Tange, Minerals 9 (2019) 745.
[47] Y.J. Zhao, J.W. Qiao, S.G. Ma, M.C. Gao, H.J. Yang, M.W. Chen, Y. Zhang, Mater. Des. 96 (2016) 10–15.
[48] J. Staun Olsen, S. Steenstrup, L. Gerward, Phys. Lett. 109A (1985) 235–237.
[49] K. Zhang, S. Peng, N.N. Li, X.Q. Liu, M.J. Zhang, Y.D. Wu, Y.P. Yang, E. Greenberg, V.B. Prakapenka, X.D. Hui, Y.D. Wang, W.G. Yang, Appl. Phys. Lett. 116 (2020) 031901.
[50] A. Jelen, J.H. Jang, J. Oh, H.J. Kim, A. Meden, S. Vrtnik, M. Feuerbacher, J. Dolinšek, Mater. Charact. 172 (2021) 110837.
[51] Y.F. Ye, Q. Wang, J. Lu, C.T. Liu, Y. Yang, Mater. Today 19 (2016) 349–362.
[52] W.A. Grosshans, W.B. Holzapfel, Phys. Rev. B 45 (1992) 5171–5178.
[53] J.C. Duthie, D.G. Pettifor, Phys. Rev. Lett. 38 (1977) 564–567.
[54] Y. Zhang, in: High-entropy Materials, Springer, Singapore, 2019, pp. 10–12.
[55] X. Gao, J. Liu, L. Bo, W. Chen, J. Sun, Z. Ning, A.H.W. Ngan, Y. Huang, Acta Mater. 277 (2024) 120203.
[56] L. Rosenkranz, Q. Lan, M. Heczko, A.J. Egan, M.J. Mills, M. Feuerbacher, U. Glatzel, J. Appl. Phys. 136 (2024) 025101.
[57] R. Soler, A. Evirgen, M. Yao, C. Kirchlechner, F. Stein, M. Feuerbacher, D. Raabe, G. Dehm, Acta Mater. 156 (2018) 86–96.
[58] M.E. Fine, Metall. Trans. A 6 (1975) 625–630.
[59] G. Fribourg, Y. Bréchet, A. Deschamps, A. Simar, Acta Mater. 59 (2011) 3621–3635.
[60] H. Wen, T.D. Topping, D. Isheim, D.N. Seidman, E.J. Lavernia, Acta Mater. 61 (2013) 2769–2782.
[61] K. Ma, H. Wen, T. Hu, T.D. Topping, D. Isheim, D.N. Seidman, E.J. Lavernia, J.M. Schoenung, Acta Mater. 62 (2014) 141–155.
[62] Z.P. Tong, H.L. Liu, J.F. Jiao, W.F. Zhou, Y. Yang, X.D. Ren, J. Mater. Process. Technol. 285 (2020) 116806.
[63] J.Z. Lu, K.Y. Luo, Y.K. Zhang, C.Y. Cui, G.F. Sun, J.Z. Zhou, L. Zhang, J. You, K.M. Chen, J.W. Zhong, Acta Mater. 58 (2010) 3984–3994.
[64] J.Z. Hao, B.J. Wang, F.X. Hu, J. Wang, J.T. Wang, H.B. Zhou, F.R. Shen, F.X. Liang, Z.B. Yu, Y.H. Gao, J.Y. Law, V. Franco, L.H. He, J. He, D. Liu, J.R. Sun, B.G. Shen, Acta Mater. 265 (2024) 119596.

Hangboce Yin
School of Materials Science and Engineering, Harbin Institute of Technology, Harbin 150001, China
CAS Key Laboratory of Magnetic Materials and Devices, and Zhejiang Province Key Laboratory of Magnetic Materials and Application Technology, Ningbo Institute of Materials Technology & Engineering, Chinese Academy of Sciences, Ningbo 315201, China

Jun-Qiang Wang
CAS Key Laboratory of Magnetic Materials and Devices, and Zhejiang Province Key Laboratory of Magnetic Materials and Application Technology, Ningbo Institute of Materials Technology & Engineering, Chinese Academy of Sciences, Ningbo 315201, China

Kai Zhang*
Center for High Pressure Science and Technology Advanced Research (HPSTAR), Shanghai 201203, China

Shu Guo
Center for Analysis and Measurement, Harbin Institute of Technology, Harbin 150001, China

Nana Li
Center for High Pressure Science and Technology Advanced Research (HPSTAR), Shanghai 201203, China

Wujing Fu
School of Materials Science and Engineering, Harbin Institute of Technology, Harbin 150001, China
Key Laboratory for Light-weight Materials, Nanjing Tech University, Nanjing 211816, China

Juntao Huo*
CAS Key Laboratory of Magnetic Materials and Devices, and Zhejiang Province Key Laboratory of Magnetic Materials and Application Technology, Ningbo Institute of Materials Technology & Engineering, Chinese Academy of Sciences, Ningbo 315201, China

Jianfei Sun
School of Materials Science and Engineering, Harbin Institute of Technology, Harbin 150001, China

Wenge Yang
Center for High Pressure Science and Technology Advanced Research (HPSTAR), Shanghai 201203, China

Yongjiang Huang*
School of Materials Science and Engineering, Harbin Institute of Technology, Harbin 150001, China

*Corresponding authors.
E-mail addresses: kai.zhang@hpstar.ac.cn (K. Zhang), huojuntao@nimte.ac.cn (J. Huo), yjhuang@hit.edu.cn (Y. Huang)

Revised 2 February 2025